

PCCP

Accepted Manuscript



This is an *Accepted Manuscript*, which has been through the Royal Society of Chemistry peer review process and has been accepted for publication.

Accepted Manuscripts are published online shortly after acceptance, before technical editing, formatting and proof reading. Using this free service, authors can make their results available to the community, in citable form, before we publish the edited article. We will replace this *Accepted Manuscript* with the edited and formatted *Advance Article* as soon as it is available.

You can find more information about *Accepted Manuscripts* in the [Information for Authors](#).

Please note that technical editing may introduce minor changes to the text and/or graphics, which may alter content. The journal's standard [Terms & Conditions](#) and the [Ethical guidelines](#) still apply. In no event shall the Royal Society of Chemistry be held responsible for any errors or omissions in this *Accepted Manuscript* or any consequences arising from the use of any information it contains.

1 Optical Extinction Efficiency Measurements on Fine and Accumulation Mode
2 Aerosol Using Single Particle Cavity Ring-Down Spectroscopy

3
4 Michael I. Cotterell,¹ Bernard J. Mason,¹ Thomas C. Preston,²

5 Andrew J. Orr-Ewing¹ and Jonathan P. Reid^{1*}

6
7 ¹ School of Chemistry, University of Bristol, Bristol, UK BS8 1TS

8 ² Department of Atmospheric and Oceanic Sciences and Department of Chemistry, McGill University,
9 805 Sherbrooke Street West, Montreal, QC, Canada H3A 0B9

10 * Author for correspondence: j.p.reid@bristol.ac.uk

11
12 A new experiment is presented for the measurement of single aerosol particle extinction efficiencies,
13 Q_{ext} , combining cavity ring-down spectroscopy (CRDS, $\lambda = 405$ nm) with a Bessel beam trap ($\lambda = 532$
14 nm) in tandem with phase function (PF) measurements. This approach allows direct measurements of
15 the changing optical cross-sections of individual aerosol particles over indefinite time-frames
16 facilitating some of the most comprehensive measurements of the optical properties of aerosol
17 particles so far made. Using volatile 1,2,6-hexanetriol droplets, Q_{ext} is measured over a continuous
18 radius range with the measured Q_{ext} envelope well described by fitted cavity standing wave (CSW)
19 Mie simulations. These fits allow the refractive index at 405 nm to be determined. Measurements are
20 also presented of Q_{ext} variation with RH for two hygroscopic aqueous inorganic systems ((NH₄)₂SO₄
21 and NaNO₃). For the PF and the CSW Mie simulations, the refractive index, n_λ , is parameterised in
22 terms of the particle radius. The radius and refractive index at 532 nm are determined from PFs, while
23 the refractive index at 405 nm is determined by comparison of the measured Q_{ext} to CSW Mie
24 simulations. The refractive indices determined at the shorter wavelength are larger than at the longer
25 wavelength consistent with the expected dispersion behaviour. The measured values at 405 nm are
26 compared to estimates from volume mixing and molar refraction mixing rules, with the latter giving

27 superior agreement. In addition, the first single-particle Q_{ext} measurements for accumulation mode
28 aerosol are presented for droplets with radii as small as ~ 300 nm.

29

30 I. Introduction

31 Aerosol can interact directly with solar radiation, perturbing how much solar energy reaches the
32 Earth's surface. Knowledge of the complex refractive index (RI), m , is central to determining the
33 scattering and absorption cross-sections of aerosol particles and the collective impact of the aerosol
34 ensemble on radiative forcing; the magnitude of the real component, n , influences the scattering of
35 light, whereas the imaginary component, k , quantifies light absorption. Atmospheric aerosols also
36 affect climate indirectly by acting as cloud condensation nuclei (CCN), impacting on the size,
37 composition and lifetime of clouds.¹ Quantifying the equilibrium partitioning of water between an
38 aerosol particle and the gas phase, and the condensational growth that results as the relative humidity
39 increases, is critical in describing the size distribution and composition of atmospheric aerosol. The
40 primary motivation for the work presented here is to report the development of a new technique for
41 reducing the uncertainties associated with the direct interaction of light with aerosol. The extinction
42 cross section of a particle, σ_{ext} , has contributions from the scattering cross section, σ_{sca} , and the
43 absorption cross section, σ_{abs} .² The ratio of σ_{ext} to the geometric cross section σ_{geo} is referred to as
44 the extinction efficiency, Q_{ext} .

45

46 Ensemble cavity ring-down spectroscopy (E-CRDS) is a well-established technique used routinely in
47 the measurement of Q_{ext} for aerosol particles with sub-micron radii.³⁻⁵ E-CRDS involves measuring
48 Q_{ext} by studying the extinction of light by a collection of hundreds to thousands of particles introduced
49 into an optical cavity formed by two highly reflective mirrors at a separation of ~ 1 m. In laboratory
50 measurements, the cloud of particles is generated using an atomiser before some degree of size
51 selection is performed prior to admitting the aerosol to the optical cavity. Rudich and co-workers
52 reported studies of absorbing aerosols using E-CRDS at a variety of visible and UV wavelengths.^{4,6,7}
53 By fitting Mie theory scattering simulations to their measured Q_{ext} trends, the authors reported trends

54 in both the real and imaginary components of the RI. Mellon *et al.* measured Q_{ext} for a range of
55 spherical and non-spherical aerosol particles at a wavelength of 1520 nm using an E-CRDS
56 technique.⁸ Meanwhile, Mason *et al.* used E-CRDS to study the size and relative humidity (RH)
57 dependence of Q_{ext} for sodium nitrate particles, and assessed the limitations inherent to E-CRDS.³
58 Most importantly, although size selection is commonplace in the E-CRDS experiments described in
59 the literature, some inevitable polydispersity in size will remain which can be difficult to characterise.
60 For all the drawbacks of E-CRDS, it has proven to be a robust technique that can be used in either the
61 laboratory or the field, and is used routinely to probe aerosol with sub-micron radii from ~500 nm
62 down to ~ 100 nm, i.e. the size regime bearing most atmospheric relevance in terms of loading and
63 light extinction.

64

65 Studying a single particle, instead of an ensemble, by combining CRDS with an independent,
66 nanometre-resolution method for determining particle size should improve the accuracy of Q_{ext}
67 measurements. Further, to satisfy the needs of the atmospheric research community, any new
68 technique for measuring Q_{ext} should retain the ability to study sub-micron particles. The motivation
69 for studying aerosol in this regime is to reduce the uncertainty associated with the influence of aerosol
70 on Earth's radiative balance.⁹ The variations of σ_{ext} , σ_{geo} and Q_{ext} with radius for spherical water
71 droplets ($n = 1.335$ at $\lambda = 532$ nm) are well known.² Importantly, the Q_{ext} curve peaks at
72 approximately 500 nm radius, highlighting the need to perform measurements in the sub-micrometre
73 regime.

74

75 The application of new techniques for the isolation and characterisation of single aerosol particles is
76 crucial in understanding aerosol processes at a fundamental level.¹⁰ Well established techniques
77 include electrodynamic balances^{11,12} and optical tweezers^{13,14}, both of which are limited to confining
78 single particles larger than 2 – 5 μm in radius. We have previously shown that a zeroth-order Bessel
79 laser beam (BB)¹⁵⁻¹⁷ optical trap can be used in the measurement of single particle processes, such as
80 evaporation and hygroscopic response, for particle radii ranging from ~ 5 μm to as small as ~ 350
81 nm.¹⁸⁻²¹ Our experience has shown that BBs can be used to trap particles smaller than 350 nm, but the

82 size of these particles cannot be determined reliably using visible light. Illuminating a particle with
83 the core of a BB will result in a radiation pressure force acting on the particle, while optical gradient
84 forces act in transverse directions to retain the particle within the core. For stable confinement, the
85 radiation pressure force may be balanced by a second counter-propagating BB, although the stability
86 of the alignment for such a system is poor.^{18,22-24} Instead, we have opted for a more robust and
87 versatile method using a counter-propagating gas flow, which exerts a Stokes drag force on a particle
88 and renders all forces balanced.^{19,20,25}

89

90 We have recently demonstrated that optical extinction measurements on single particles can be made
91 using a BB ($\lambda = 532$ nm) to control the position of a single aerosol particle within a CRD beam.^{20,25,26}

92 By observing how the presence of a particle in the centre of the CRD beam changes the rate of decay
93 of light from the high finesse optical cavity formed by two highly reflective mirrors, σ_{ext} values for
94 aerosols have been determined at a laser wavelength of 532 nm. In tandem with size determination
95 from angular light scattering measurements, the variation of Q_{ext} was measured for the simple case of
96 slowly evaporating 1,2,6-hexanetriol droplets²⁵ and for the more complicated case of hygroscopic
97 growth of sodium chloride droplets.²⁰ Not only does optical confinement of a single particle remove
98 the assumptions inherent in E-CRDS measurements and improve the size determination accuracy, but
99 it also allows the same single particle to be studied over a long period of time. This latter advantage
100 permits the optical cross-section to be studied as a particle changes sizes or composition due to, for
101 example, the evaporation of semi-volatile species, the uptake of water if the RH in the chamber
102 increases, or even the chemical transformation accompanying heterogeneous aging.

103

104 Our previous publications^{20,25} are based on experiments using a CRD beam wavelength of 532 nm,
105 which was chosen in part for experimental convenience but also because it is close to the measured
106 maximum in the solar spectrum at sea level. Measurements were limited to particles with radii larger
107 than ~ 750 nm, outside the atmospherically-relevant accumulation mode regime (< 500 nm). It is
108 important that the range of wavelengths for which Q_{ext} is measured is extended to the UV and IR
109 regions of the spectrum, to assess the impact of aerosols on the radiative balance at these wavelengths,

110 and that measurements be made for accumulation mode particles. At shorter wavelength and, thus,
111 larger size parameter, the number of features in a Q_{ext} resonance spectrum increases, improving the
112 accuracy with which RI determinations can be made. At longer wavelengths (towards the IR region),
113 water begins to absorb significantly, possibly allowing the effect of the imaginary RI component on
114 the Q_{ext} spectrum to be explored. Further, our previous studies for hygroscopic growth of aerosols
115 containing inorganic species did not report independent fits of the RI, but instead employed the
116 parameterisations of Tang and Munkelwitz. Although providing a validation of previous results, this
117 approach did not represent a strategy for determining the optical properties and hygroscopic response
118 of aerosol of completely unknown RI and composition.²⁷

119

120 The purpose of this publication is many fold. A new experiment is presented: although broadly similar
121 to our single particle 532 nm CRDS apparatus detailed previously,^{20,25} CRDS measurements are
122 performed at a wavelength of 405 nm allowing us to quantify the dispersion in RI between 532 and
123 405 nm. This new set-up is benchmarked by determination of Q_{ext} variation for 1,2,6-hexanetriol
124 droplets; comparison with cavity standing wave (CSW) Mie theory calculations allows the constant
125 RI of hexanetriol at $\lambda = 405$ nm to be extracted. Further, we describe a new method of fitting both the
126 angular variation in elastically scattered light and the CRDS data for hygroscopic growth
127 measurements to determine the RI of aerosol particles directly with no prior assumptions.
128 Subsequently, CRDS measurements and RI determinations for the hygroscopic growth of ammonium
129 sulfate and sodium nitrate droplets are presented. The resulting independent determinations of RI as a
130 function of RH are compared with previous literature parameterisations, in addition to volume
131 fraction and molar refraction mixing rules. Finally, using the previously described 532 nm CRDS
132 apparatus^{20,25} with a reduced BB core, the first single particle measurements of Q_{ext} for droplets with
133 radii as small as ~ 250 nm are reported.

134

135 **II. Experimental**

136 The experimental apparatus for the 532 nm CRDS system has been described elsewhere;^{20,25} the new
137 405 nm CRDS system is similar in design, and is described here and summarised in Figure 1. The

138 beam from a 35 mW, single mode 405 nm diode laser (IQ Series, Power Technology Incorporated)
139 was passed through an acousto-optic modulator (AOM, Brimrose) which split the beam into a series of
140 diffraction spots. The first order diffraction spot was selected and injected into an optical cavity, while
141 the zeroth and higher order spots were directed into a beam dump. The optical cavity was constructed
142 from two highly reflective mirrors (Layertec) with reflectivities greater than 99.96 % at 405 nm and
143 radii of curvature of 1 m, separated by a distance of 0.8 m. One mirror was mounted on a piezo ring
144 actuator (Piezomechanik), driven with a triangular waveform of amplitude 20 V at a fixed frequency
145 in the range 10 – 20 Hz. Build-up of light inside the cavity was monitored using a photodiode
146 (RedWave Labs, D101), and the intensity escaping the cavity was measured as an output voltage
147 which was sent to both a Compuscope 12-bit digitizer (GaGe, Octopus CS8222) and a digital delay
148 generator (Quantum Composers, Sapphire 9200). The digital delay generator sent a 5 V TTL pulse to
149 the AOM when the voltage reached a pre-selected threshold, causing the first order diffraction beam
150 from the AOM to extinguish, hence initiating a ring-down decay.

151

152 To reduce the impact of light scattering by airborne dust particles on ring-down times (RDTs) and to
153 prevent the mirrors getting dirty, nitrogen gas purge flows were directed across the faces of the cavity
154 mirrors and through flow tubes which extended from the mirror faces to the trapping cell at the centre
155 of the cavity. The cavity was aligned such that the TEM₀₀ mode was preferentially excited; as a result,
156 higher order modes with lower coupling efficiencies, and hence lower amplitude ring-down events,
157 could be discriminated against in the data collection. The subsequent TEM₀₀ mode ring-down traces of
158 photodiode voltage (V) vs time (t) were fitted to a single exponential function of the form
159 $V = V_0 \exp(-t/\tau) + b$ where b accounts for any baseline offset, and τ is the RDT, which was
160 recorded at a rate of between 5 and 10 Hz. In the case of the empty cavity purged with N₂ gas, this
161 RDT is denoted τ_0 , and typically has a value of $14.5 \pm 0.5 \mu\text{s}$ depending on the cleanliness of the two
162 cavity mirrors and their alignment, although remains constant over the course of a measurement with a
163 typical standard deviation $< 0.1 \mu\text{s}$.

164

165 A 532 nm Gaussian laser beam (Laser Quantum 2W Opus) was passed through a 2° axicon (Altechna)
166 to produce a Bessel beam. Immediately after the axicon, the BB core diameter was measured to be 55
167 μm , which is too large to trap micron-sized aerosol particles.¹⁸ Hence, a pair of lenses was used to
168 reduce the core diameter to $\sim 5.5 \mu\text{m}$. This beam was propagated vertically into the trapping cell using
169 a 45° mirror. The mirror and the trapping cell were mounted on a translation stage. The radiation
170 pressure exerted by this vertically propagating BB on a trapped particle was balanced by a humidified
171 nitrogen gas flow of 100 - 200 sccm, the RH of which could be controlled. This gas flow was also
172 used to purge the cell of excess aerosol. The RH inside the trapping cell was monitored using a
173 capacitance probe (Honeywell). A camera coupled to a 20 \times long working distance objective with a
174 numerical aperture (NA) of 0.42 was used to capture the angular variation of elastically scattered light
175 (phase function) with *s*-polarisation from a single trapped aerosol particle. Aerosol particles were
176 introduced into the cell via a medical nebuliser (Omron). If multiple particles were trapped, the
177 trapping cell was evacuated and aerosol was again nebulised into the cell. This process was repeated
178 until only a single particle was trapped.

179

180 Once a single aerosol particle was optically trapped, its position was optimised to obtain a minimum in
181 the measured RDTs. The position could be tuned in both transverse directions to the CRD beam, in the
182 vertical direction by changing the laser power and in the horizontal direction by scrolling the
183 translation stage on which the trapping cell was mounted. When the particle was centred in the CRD
184 beam, laser feedback control was initiated to keep the particle in the centre over the course of the
185 measurement, and RDTs were collected for the particle in the CRD beam, denoted by τ . Typically, the
186 power of the laser required modulating between 400 and 2000 mW over the course of an experiment,
187 depending on the size and composition range of the droplet levitated. From measured τ and τ_0 values,
188 the optical cross section was calculated using Equation 1, in which L is the cavity length, c is the speed
189 of light and w is the CRD beam waist.^{28,20}

$$\frac{1}{\tau} - \frac{1}{\tau_0} = \frac{2c\sigma_{ext}^*}{L\pi w^2} \quad \text{Equation 1}$$

190 Although w can be predicted using geometric optics (see Kogelnik and Li²⁹), giving an approximate
191 value, w is in practice treated as a fitting parameter in all σ_{ext} simulations. Note that the asterisk in σ_{ext}^*
192 indicates the measured extinction cross section in a cavity standing wave, as opposed to a travelling
193 wave which is assumed in Mie theory. Miller and Orr-Ewing calculated the effect of the standing wave
194 on the observed scattering cross-section of an aerosol particle.³⁰ They showed that the effect of the
195 standing wave on the measured extinction cross-section σ_{ext}^* is encapsulated in a phase parameter, ζ ,
196 which relates σ_{ext}^* to the Mie theory value, σ_{ext} :

$$\sigma_{ext}^* = \zeta(m, a, z_0)\sigma_{ext} \quad \text{Equation 2}$$

197 Here, ζ is a function of the position of the particle with respect to the phase of the standing wave, z_0 , as
198 well as the RI and size of the particle. Miller and Orr-Ewing showed how ζ may be calculated when a
199 particle is centred on a node and on an anti-node of an intra-cavity standing wave, which form the two
200 limiting cases in the distribution of measured σ_{ext}^* data.³⁰ Here, we refer to this modification of Mie
201 theory as cavity standing wave (CSW) Mie theory. Experimental verification of the effect of the
202 standing wave on the measured σ_{ext}^* , and the importance of taking into account CSW Mie theory were
203 demonstrated by Mason and co-workers.^{25,26}

204

205 Once the optical cross-section has been determined, the radius of the particle must be measured to
206 calculate Q_{ext} . The radius of the particle is determined from the phase function (PF) image, which is
207 analysed to give the one dimensional relative intensity distribution with scattering angle. This
208 distribution is affected not only by particle radius but also by the RI of the particle. Measuring the
209 angular variation in the scattered intensity and simulating the measured distribution using Mie theory
210 provides a method of obtaining the particle size and RI, even for sub-micron aerosol particles.³¹

211

212 III. Optical Extinction Measurements for 1,2,6-hexanetriol droplets

213 To benchmark the experiment and assess its capability, it is important to measure σ_{ext}^* for a spherical
214 particle of constant composition (RI) over a continuous size range and determine whether the data can

215 be described using CSW Mie theory. Hexanetriol is a semi-volatile organic compound that is
216 relatively non-hygroscopic, particularly when compared to the water uptake of inorganic species such
217 as sodium chloride in high RH environments. Although having no atmospheric relevance, it serves as
218 an ideal system to benchmark our experiment, and has been studied extensively in previous
219 work.^{20,19,25,26} A hexanetriol droplet was optically trapped at low RH (< 10%), and its position in the
220 CRD beam optimised. The RDTs and PFs were subsequently measured over ~ 2 hours as the particle
221 evaporated.

222

223 The radius, a , and constant RI of a droplet were determined from the PFs by comparing to a computed
224 library of Mie-theory simulated PFs over a defined radius range for a constant value of the real
225 component of the RI, n_{532} . The Pearson correlation coefficient, C , between each of the simulated and
226 measured PFs was calculated. For each measured PF, the simulation with the highest correlation
227 defined the best-fit radius of the particle for the corresponding value of n_{532} . Once the radii were
228 determined for all the measured PFs in an entire data set, the mean correlation coefficient \bar{C} is
229 calculated for the value of n_{532} of the first iteration before varying n_{532} in a stepwise manner. Note that
230 \bar{C} is defined as the arithmetic mean of the collection of Pearson correlation coefficients calculated for
231 the entire data set for the particular trial value of n_{532} . Then, by identifying the n_{532} that yielded the
232 maximum \bar{C} calculated over the full range of trial values of n_{532} , the best-fit constant RI for
233 hexanetriol was determined.

234

235 The radius data for 10 such measurements are shown in Figure 2(a); the largest droplet was initially
236 trapped at a radius of 2140 nm, and the smallest droplet evaporated to a size of 725 nm. The inset
237 shows how the mean correlation coefficient, \bar{C} , between the experimental and simulated PFs varies
238 with n_{532} for one of the droplets (plotted using red data points). For this particular droplet, the best fit
239 n_{532} peaks at ~ 1.481; the average determined RI for all 10 droplets is 1.477 ± 0.004 where the error
240 represents one standard deviation. This value of n_{532} for hexanetriol is consistent with previous
241 measurements using either single aerosol particle CRDS (1.4782 ± 0.0007)²⁵ at 532 nm, or a

242 combination of radiation pressure and PF measurements (1.482 ± 0.001)¹⁹. We will now focus on the
243 particle that has been highlighted in more detail.

244

245 Figure 2(b) shows the Q_{ext} values inferred from the CRDS measurements at 405 nm as a function of
246 particle radius, with the radius and geometric cross-section determined from the PF measurements.
247 The CSW Mie simulations of Q_{ext} are performed for the two limiting cases of the particle centred at a
248 node and anti-node. These simulations depend on the RI at 405 nm; although n_{532} is known from the
249 PF fitting, n_{405} is not known but can be determined by varying it as a fit parameter. In addition, the
250 CRDS beam waist is varied, which has the effect of scaling the measured Q_{ext} data to larger or smaller
251 values (i.e., an amplitude shift in Q_{ext}) as would be expected after inspection of Equation 1. We define
252 a residual as the fraction of the measured Q_{ext} points that fall outside the simulation envelope, and this
253 residual is minimised by varying w and n_{405} . Accordingly, Figure 2(b) shows the best fit CSW Mie
254 theory simulations for the limiting node and anti-node cases. The inset to Figure 2(b) shows an
255 expanded portion of these Q_{ext} data accompanied with a conventional Mie theory simulation (solid
256 yellow line). This inset emphasises how the measured Q_{ext} data are broadened by the impact of the
257 cavity standing wave, with the Q_{ext} being scaled in equal proportion to higher and lower values about
258 this Mie theory curve. It also emphasises how well the CSW Mie theory simulations describe the
259 boundaries of this broad Q_{ext} envelope. Note that in previous publications where both the PF and the
260 CRD data were measured at the same wavelength (532 nm), the droplet radius was scaled using an
261 empirical formula when the RI was varied to correct for using an inaccurate RI in the PF fitting.²⁵ This
262 method cannot be used here because the PF and CRD data are measured at different wavelengths.
263 Nonetheless, the agreement in the peak positions between the measured Q_{ext} data and the CSW Mie
264 simulations is remarkable, indicating that the radius determination from the PF fitting is more accurate
265 than for our previous single particle CRDS measurements.²⁵

266

267 Figure 2(c) shows a contour plot of the residual variation with n_{405} and w used in the CSW Mie
268 simulations, with a region where the residual is minimised. Figure 2(d) shows an expanded portion of
269 this contour plot in which a finer grid search was performed. In this expanded portion, local minima

270 can be seen because of the noise inherent in the measured Q_{ext} data. The best fit is defined as the
271 midpoint of the contour where the residual rises above the baseline noise (shown by the thicker line in
272 the figure). The best fit has 34.5% of points lying outside the simulated envelope, and gives $w =$
273 $259.15 \pm 0.2 \mu\text{m}$ and $n_{405} = 1.48875 \pm 0.0005$. Note that only the real component of the RI is varied,
274 and k is set to zero. The determined beam waist is in good agreement with the prediction of $253 \mu\text{m}$
275 obtained using theory for symmetrical resonators.²⁹ The large value for the minimum in the residual is
276 due to large contributions where the envelope in Q_{ext} narrows; where the CSW Mie simulations for the
277 limiting node and anti-node cases cross, there is scatter in Q_{ext} deriving from noise in both τ and τ_0 .

278

279 Each of the radius-time data sets in Figure 2(a) has corresponding RDT data, which were analysed to
280 determine w and n_{405} for all 10 particles. The mean value of n_{405} is 1.4906 ± 0.0012 , while the mean
281 value of w is $264.4 \pm 4.4 \mu\text{m}$, where the errors represent one standard deviation in the measured
282 values. The former mean value is in good agreement with previous determinations of n_{405} for
283 hexanetriol using radiation pressure measurements, which gave a value of 1.485 ± 0.006 .¹⁹ The
284 percentage error in w is much larger than that in n_{405} , which is expected; from one day to the next, the
285 cavity alignment can drift and needs re-alignment. The measured n_{405} values are larger than the n_{532}
286 values measured from the PFs and those reported previously by Mason and co-workers ($1.4782 \pm$
287 0.0007), in accordance with the dispersion trends exhibited by most substances.²⁵ Further, both the n_{405}
288 and n_{532} values are higher than refractometer (Misco, Palm Abbe II) measurements which give a bulk
289 RI of 1.4758 at a wavelength of 589.6 nm.

290

291 **IV. Fitting Refractive Index for Hygroscopic Inorganic Species**

292 The analysis of the PF and RDT data for hexanetriol was relatively straightforward: each droplet has a
293 composition (and hence RI) that does not change over time, assuming the RH remains constant at 0%.
294 In this section, we look at measurements and the analysis of the PF and RDT data for hygroscopic
295 inorganic salts as the ambient RH is varied. A changing RH results in the condensation or evaporation
296 of water from a hygroscopic droplet. As a consequence, both the size and composition of the droplet
297 change, leading to a size dependent RI. An aqueous inorganic salt solution with a typical solute

298 concentration of 100 gL^{-1} was nebulised into the trapping cell, and a single aqueous droplet optically
299 trapped in the BB core at a high RH ($>70\%$). The position of the droplet was optimised until it was
300 located at the centre of the $\lambda = 405 \text{ nm}$ CRD beam. The PFs and RDTs were collected while the RH
301 was lowered steadily over time. In the following sections, we initially describe our PF fitting strategy
302 for the determination of both radius and RI for hygroscopic growth measurements before
303 demonstrating the ability to retrieve the RI at wavelengths of 405 nm and 532 nm for ammonium
304 sulfate and sodium nitrate aerosol droplets. Finally, we test common literature mixing rules to assess
305 their validity in predicting the variations of RI with relative humidity.

306

307 *IV. a Strategy for fitting PFs for hygroscopic growth measurements*

308 Previous radius determinations from PFs in the literature used either a fixed RI, or modelled a varying
309 RI by linking the composition of a particle to its radius or the RH of the surrounding environment^{20,19}
310 using the parameterisations of Tang and Munkelwitz.²⁷ However, with recent improvements in the
311 acquisition of PFs (in particular, noise reduction), as well as computational advances in fitting the PFs
312 to Mie theory, we are now in a position to fit both the RI and the particle radius.³² In principle, a
313 suitable approach to characterising a trapped particle is to find values of a and n that maximise the
314 correlation between experimental and simulated PFs. In practice, even when a particle is homogeneous
315 and spherical, this method yields best-fits that contain high uncertainties. Typically, the poor quality of
316 the fits is noticeable when the analysis is applied to a series of PFs measured under experimental
317 conditions where both a and n should change slowly over time. When these measurements are fitted
318 and the results are plotted as a function of time, both a and n can be scattered and contain
319 discontinuities that are contrary to the expectation that their change over time should be smooth.
320 Needless to say, analysis and interpretation of these types of data are difficult.

321

322 To reduce, or perhaps eliminate, the above problem, an alternative fitting scheme is implemented here.
323 For a PF data set acquired for one droplet over a long time frame, the Pearson correlation coefficient C
324 is maximised with respect to a over the whole data set, constraining the relationship between radius
325 and n by the equation:

$$n = n_0 + \frac{n_1}{a^3} + \frac{n_2}{a^6} + \dots + \frac{n_k}{a^{3k}} \quad \text{Equation 3}$$

326 Of these parameters, only n_0 is known beforehand (the refractive index of pure water at the
327 wavelength of the measurement), while n_1, n_2, \dots, n_k must still be determined. These additional terms
328 are found by maximising the mean correlation coefficient \bar{C} across an entire set of PFs (for
329 experiments performed here, there will typically be several thousand PFs in a data set). Maximised
330 correlation coefficients between experimental and simulated PFs are found by fixing n_1, n_2, \dots, n_k
331 across all PFs and varying a in fitting each individual PF in the set. The resulting set of maximised
332 correlation coefficients is then used to calculate \bar{C} for the chosen parameter set and represents one
333 point on the k -dimensional space formed by n_1, n_2, \dots, n_k . The goal is to find the point in this space
334 that maximizes \bar{C} and, in this work, a grid-search is used to accomplish this task.³³ After each
335 calculation of \bar{C} , one of the parameters n_1, n_2, \dots, n_k is incremented using a chosen step size and \bar{C}
336 is calculated once more. This process is repeated until a maximum in the correlation coefficient is
337 located. The point in the k -dimensional grid that maximises \bar{C} corresponds to the best-fit values for
338 parameters n_1, n_2, \dots, n_k (the values of a for each PF are found during the calculation of \bar{C} for this
339 point). During testing, this method was found to reduce both noise and discontinuities in a and n . Note
340 that the quality of the fits is also found to improve when both the lower and upper values of the
341 angular range for the measured PFs are allowed to vary for each individual PF by 1.5° to account for
342 changes in the computer-determined positions of the droplet edges during image processing.

343

344 When the particle radius is infinitely large (i.e. at infinite RH or dilution of solutes), Equation 3
345 simplifies to $n = n_0$; thus n_0 corresponds to the RI value for a pure water droplet, which is 1.335 at
346 532 nm. The terms n and $n_0, n_1, n_2, \dots, n_k$ are wavelength dependent and will be denoted as
347 $n_\lambda, n_{0,\lambda}, n_{1,\lambda}, n_{2,\lambda}, \dots, n_{k,\lambda}$ from this point forward. The $n_{k,\lambda}$ values will vary from one experiment to
348 another depending on the mass of solute in the droplet, while the number of terms required to model

349 accurately the RI will also vary, although typically only $n_{1,\lambda}$ and $n_{2,\lambda}$ are required. Initial ranges are
350 set for $n_{1,532}$ (typically between 0 and $1 \times 10^9 \text{ nm}^3$ for radii $< 2 \text{ }\mu\text{m}$) and $n_{2,532}$ (between -3 and 3×10^{18}
351 nm^6), with $n_{1,532}$ optimised initially while $n_{2,532}$ is set to zero. \bar{C} is determined for every iteration of
352 $n_{1,532}$, with the highest \bar{C} corresponding to the optimum value of $n_{1,532}$. Next, $n_{2,532}$ is varied with
353 $n_{1,532}$ set to its optimum value. After these initial optimisations, refining grid search cycles are
354 performed with the steps in the grid search being reduced by 50% after every search cycle.

355

356 *IV. b Hygroscopic growth measurements for ammonium sulfate*

357 Our initial discussion focuses on a hygroscopic growth measurement for an ammonium sulfate droplet,
358 which was trapped at $\sim 80 \text{ \% RH}$; the ambient RH was subsequently lowered to $\sim 38\%$, at which point
359 the droplet fell out of the trap following crystallisation. Figure 3(a) shows how \bar{C} changes as $n_{1,532}$
360 (red squares) and $n_{2,532}$ (blue circles) are varied during their initial optimisation stages. The \bar{C} values
361 for the $n_{2,532}$ optimisation stage are higher as a result of $n_{1,532}$ having been optimised, and $n_{2,532}$
362 representing a small perturbation of the curve in n_{532} / a^{-3} space. Figure 3(b) shows the final radius-
363 time determination (after the refining grid search cycles) corresponding to $\bar{C} = 0.9701$, accompanied
364 by the variation in the RH over the measurement. The inset shows the final, best-fit RI curve as a
365 function of a^{-3} , and the impact of the variation of the $n_{2,532}$ term can be clearly seen by the curvature
366 in this plot. The values of $n_{1,532}$ and $n_{2,532}$ for this particular droplet are $8.84 \times 10^8 \text{ nm}^3$ and
367 $-2.12 \times 10^{18} \text{ nm}^6$ respectively. Note that a small perturbation from a third-order term, $n_{3,532}$, was also
368 applied with a value of $2.00 \times 10^{27} \text{ nm}^9$ in order to refine further the RI description. The uncertainties in
369 these values are difficult to quantify. However, we show later that the determined RI description
370 behaves as expected when compared to parameterisations by Tang et al.^{27,34} The radius-time data
371 decrease smoothly with very little experimental noise, and only exhibit a couple of discontinuities in
372 the droplet radius, each with a magnitude of $< 5 \text{ nm}$. The low noise and smooth variation in the radius

373 suggest that the improvements in the PF acquisition and subsequent Mie theory fitting procedure have
 374 resulted in better-quality radius determination compared to other published determinations from PFs of
 375 sub- 2 μm droplets.^{20,19,35}

376

377 Now the radius of the particle has been determined, Q_{ext} may be calculated from the RDT data for a
 378 trial beam waist, which will later be treated as a fitting parameter. Knowing for certain the droplet
 379 size, simulating the Q_{ext} data with CSW Mie theory allows a retrieval of the variation in n_{405} with
 380 particle radius, leading to direct measurements of the dispersion in RI. We generate another expression
 381 of the form of Equation 3, but instead of using a value of $n_{0,532} = 1.335$, we now fix the RI of water to
 382 the known value of $n_{0,405} = 1.343$.³⁶ Further, instead of fitting $n_{1,405}$ and $n_{2,405}$, we use:

$$n_{405} = n_{0,405} + \frac{n_{1,532} + \Delta n_1}{a^3} + \frac{n_{2,532} + \Delta n_2}{a^6} + \frac{n_{3,405}}{a^9} \quad \text{Equation 4}$$

383 where $n_{1,532}$, $n_{2,532}$ and $n_{3,532}$ have been determined by the PF fitting procedure, and small offsets to
 384 these first-order (Δn_1) and second-order (Δn_2) coefficients are applied with the fitting at 532 nm
 385 thereby providing excellent first estimates of the values. Therefore, fitting the Q_{ext} data to CSW Mie
 386 simulations requires a three parameter fit, varying w , Δn_1 and Δn_2 using a grid searching approach.
 387 Owing to the computational time needed to perform this fitting, no offset is applied to the third order
 388 $n_{3,532}$ term.

389

390 Unlike the experiments involving hexanetriol, as the RH variation is not perfectly linear in
 391 hygroscopic growth measurements (particularly evident at the beginning of the measurement in Figure
 392 3(b)), the ‘density’ of the measured Q_{ext} data points is not uniform in the radius domain. To ensure
 393 there is no bias in the fitting of CSW Mie simulations to higher density regions of Q_{ext} data, the values
 394 of Q_{ext} are collected into 1 nm bins and each point that falls outside the envelope is weighted by
 395 dividing by its associated bin’s number count. The result of the fitting of CSW Mie theory simulations
 396 to the Q_{ext} data is shown in Figure 4(a). Not only is there excellent agreement in the resonance peak
 397 positions of the measured Q_{ext} and CSW Mie simulations (further indicating accurate size

398 determination of the droplet from PF analysis), but there is also a good description of the underlying
399 contour of the data (indicating good determination of the variation in n_{405} over the measurement).

400

401 Figure 4(b) shows a contour plot of the residual in terms of Δn_1 and Δn_2 , which exhibits a definite
402 minimum, with several local minima resulting from noise in the Q_{ext} data. The values of Δn_1 and Δn_2
403 corresponding to a minimum in the residual are $(0.95 \pm 0.03) \times 10^8 \text{ nm}^3$ and $(4.4 \pm 0.2) \times 10^{16} \text{ nm}^3$,¹⁷
404 respectively, with uncertainties determined by the distance to the contour where the residual rises
405 above the baseline noise. Note that the well in the residual is diagonal in shape, implying that Δn_1 and
406 Δn_2 are inversely correlated, while the uncertainties in Δn_1 and Δn_2 may also be correlated. In a
407 similar way, w is found to be $251.5 \pm 0.5 \text{ }\mu\text{m}$.

408

409 The parameterisation of the variation of n_{532} and n_{405} with RH may be of value for applications in
410 environmental research. Therefore, polynomial fits to the measured n_{405} and n_{532} variation with water
411 activity, a_w , used Equation 5, where C_i are polynomial coefficients, the values of which are reported in
412 Table 1:

$$n_\lambda = \sum_{i=0}^4 C_i a_w^i \quad \text{Equation 5}$$

413 The uncertainties quoted in Δn_1 and Δn_2 allow the uncertainty envelope in n_{405} to be calculated.
414 When parameterising n_{405} in the RH domain, these uncertainties in Δn_1 and Δn_2 are negligible when
415 compared to the errors associated with the RH measured ($\pm 2\%$). This point is emphasised in Figure
416 4(c) which shows the dependence of n_{405} (purple solid line) and n_{532} (black data points) on RH. The
417 narrow red envelope represents the uncertainty in n_{405} if we only consider the errors obtained by fitting
418 the Q_{ext} data, while the broad grey envelope takes into account the uncertainty in the RH probe
419 measurement. Clearly, the $\pm 2\%$ uncertainty in the RH probe measurement is the dominant source of
420 error in any RI – RH parameterisation. A comparison is also made to the parameterisation of Tang *et*
421 *al.* (red solid line) determined at a wavelength of 632.8 nm.^{27,34} The measured n_{532} curve from the PF
422 measurements is shifted towards higher RI compared to the Tang parameterisation, while the n_{405}

423 curve is shifted towards higher RI relative to n_{532} (as expected given typical wavelength dispersion
424 behaviour). Further, the separation between the n_{405} and n_{532} curves increases as the RH is lowered and
425 the droplet composition tends to that of the solute, which is also expected given the higher chromatic
426 dispersion of inorganic salts compared to water.

427

428 *IV. c Hygroscopic growth measurements for sodium nitrate*

429 Sodium nitrate aerosol is another atmospherically relevant system; NaNO_3 particles form by the
430 reaction of sea salt aerosol with nitric acid and NO_x , and can impact the radiative forcing in marine
431 environments.³⁷ There is ongoing debate over the hygroscopic properties and the RH at which NaNO_3
432 droplets effloresce, with Gysel *et al.* not observing any efflorescence at RHs as low as $\sim 6\%$ using an
433 ensemble technique.³⁸ Thus, single NaNO_3 droplets were confined within a Bessel laser beam and
434 placed into the centre of our 405 nm CRD beam for the measurement of Q_{ext} with variations in RH.

435

436 Figure 5(a) shows the measured Q_{ext} variation with radius for one droplet which fell from the trap at \sim
437 12% RH, although the particle loss may not be a consequence of efflorescence. Instead, the
438 combination of both the small size of the droplet and its RI may have rendered the forces acting on it
439 too weak for stable trapping. The measured Q_{ext} is again very well described by CSW Mie theory.
440 Both the resonance peak positions and the underlying contour of the Q_{ext} curve agree well with the
441 CSW Mie simulations. This agreement is indicative of correct size determination of the particle by PF
442 analysis at 532 nm, as well as good determination of the variation of n_{532} and n_{405} with changing RH.
443 The values of $n_{1,532}$, $n_{2,532}$ and $n_{3,532}$ for this particular droplet are $2.28 \times 10^8 \text{ nm}^3$, $-3.28 \times 10^{16} \text{ nm}^6$
444 and $1.20 \times 10^{25} \text{ nm}^9$ respectively. The values of Δn_1 and Δn_2 corresponding to the minimum in the
445 contour plot of Figure 5(b) are $(4.48 \pm 0.03) \times 10^7 \text{ nm}^3$ and $(-3.2 \pm 0.1) \times 10^{16} \text{ nm}^{17}$ respectively. Figure
446 5(c) compares the n_{532} determined from our measurement with Tang's parameterisation ($\lambda = 633 \text{ nm}$),
447 with an expected shift in n_{532} towards higher RI not observed.²⁷ Further, the n_{405} variation with RH is
448 displaced to higher values compared to the n_{532} curve, as expected. The similarity in the n_{532} and n_{633}
449 curves suggests that the refractive index dispersion is a weak function of wavelength until the blue

450 region of the spectrum is reached. Again, a polynomial was fitted to the measured n_{405} and n_{532}
451 variation with water activity using Equation 5, and the coefficients are presented in Table 1 along with
452 those for $(\text{NH}_4)_2\text{SO}_4$.

453

454 *IV. d Comparison of determined RIs with literature mixing rules*

455 Figure 6 summarises the variation of n_{405} with RH for both the $(\text{NH}_4)_2\text{SO}_4$ and NaNO_3 droplets studied
456 (purple solid lines). These variations can be compared with predictions from refractive index mixing
457 rules, with the two most common being the volume fraction weighting and the molar refraction
458 methods. The volume fraction mixing rule is widely encountered,^{39,40} and uses a volume fraction
459 weighting of the pure solute, n_s , and pure water, n_w , RIs as shown in Equation 6 where ϕ_s is the
460 volume fraction of solute.

$$n = \phi_s n_s + (1 - \phi_s) n_w \quad \text{Equation 6}$$

461 The volume fraction of solute can be calculated from the mass fraction of solute, m_s , provided the
462 densities of the pure solute, ρ_s , and pure water, ρ_w , are known.

$$\phi_s = \frac{m_s \rho_w}{m_s (\rho_w - \rho_s) + \rho_s} \quad \text{Equation 7}$$

463 Although ρ_w is well known at 25 °C, the densities of pure liquid inorganic substances at 25 °C and
464 atmospheric pressure cannot be measured. However, Clegg and Wexler calculated these values for
465 numerous inorganic solutes, including $(\text{NH}_4)_2\text{SO}_4$ and NaNO_3 .⁴¹ The variation of n_{405} with m_s can now
466 be calculated, taking n_{405} for water to be 1.343 and n_{405} for the pure solute to be the value of C_0 in
467 Table 1 (i.e. the extrapolated value from the measured n_{405} curve to RH = 0%). Finally, the Extended
468 Aerosol Inorganics Model (E-AIM) is used to relate m_s to the RH.⁴²

469

470 The molar refraction mixing rule uses a mole fraction, x , weighting of the molar refraction, R , as
471 described by Equation 8 and 9 where M is the molecular mass.³⁹

$$R = x_s R_s + (1 - x_s) R_w \quad \text{Equation 8}$$

$$R = \frac{(n^2 - 1)M}{(n^2 + 2)\rho} \quad \text{Equation 9}$$

472 Again, the value of n_{405} for water is taken as 1.343 and n_{405} for the pure solute as the appropriate C_0 in
 473 Table 1. Further, the Clegg and Wexler model⁴¹ is used to describe the variation in density with m_s ,
 474 while the E-AIM model is used to relate mass fraction to the RH.⁴² The RH-dependencies of these two
 475 mixing rule models are presented in Figure 6 for both $(\text{NH}_4)_2\text{SO}_4$ and NaNO_3 , and compared against
 476 the respective measured variation of n_{405} . The dashed black line in Figure 6 for $(\text{NH}_4)_2\text{SO}_4$ is the RH
 477 variation of n_{405} predicted by the volume fraction mixing rule when density and pure component n_{405}
 478 are taken as the typical values implemented in radiative transfer models. In this case, the crystalline
 479 $(\text{NH}_4)_2\text{SO}_4$ density (1.769 g cm^{-3}) is used, while n_{405} for pure $(\text{NH}_4)_2\text{SO}_4$ is taken as 1.54, based on
 480 values recommended for radiative transfer modelling by the appraising direct impacts of aerosol on
 481 climate (ADIENT) database.⁴³ There are no recommended values of RI for NaNO_3 . Clearly, the molar
 482 refraction mixing rule gives a very good description of n_{405} for both inorganic systems, while the
 483 conventional volume fraction mixing rule gives a poor description.³⁹ The molar refraction mixing rule
 484 is self-consistent with the Lorentz-Lorenz relation, a fundamental description of how the RI of a bulk
 485 material is related to its polarisability, while the volume fraction mixing rule has no physical basis.

486

487 *IV. e Further investigation of sodium nitrate's behaviour at low (< 10 %) RH*

488 In this section, we demonstrate that sodium nitrate aerosol does not always effloresce at low (< 10 %)
 489 RH. The reproducibility in Q_{ext} can therefore be studied by cycling the RH between high (> 60 %) and
 490 low values, which is of particular interest at low RH because the viscosity of sodium nitrate aerosol
 491 might reach appreciably high values. Thus, another aqueous NaNO_3 droplet was subjected to detailed
 492 study, although in this instance the CRDS data were acquired at a wavelength of 532 nm using the
 493 apparatus described in previous publications.^{20,25,26} As shown in the inset of Figure 7(a), the trapping
 494 cell RH was initially at $\sim 75\%$ and was subsequently lowered and then held at an RH of $\sim 2\%$ for ~ 40
 495 minutes. Over this measurement period, size determination from the PFs was reasonable (also shown
 496 in the inset to the figure) albeit with $\sim 20 \text{ nm}$ jumps in the particle radius at regular intervals, and the

497 droplet radius steadily reduced. During the ~ 40 minute period at low RH, the droplet did not undergo
498 efflorescence and remained trapped, with the size of the droplet stable. The RH was increased to high
499 ($\sim 66\%$) RH, and then back to low RH to investigate the possibility that there might be hysteresis in
500 the droplet's RDT and Q_{ext} data, in particular at the high viscosities anticipated at low RH. The cycling
501 of the RH also allows us to examine the reproducibility in the determination of the optical properties
502 of the aerosol. The resulting RDT values are shown as a function of time in the main panel of Figure
503 7(a).

504

505 There is clear symmetry in the RDTs as the RH is cycled between high and low RH. The three
506 different phases to the RH cycling are now separately analysed in more detail, although the radius was
507 determined from analysing all the PFs together for the three phases. These three phases are the first
508 4000 s during which the RH is initially lowered; 4000 – 8000 s in which the RH is subsequently
509 increased; and 8000 s to the end of the measurement, for which the RH is once again lowered to ~ 3
510 %. These three phases are shown in the three panels of Figure 7(b). There are a few mismatches in
511 resonance peak locations in all cases resulting from the ~ 20 nm jumps in the radius data, although
512 there is reasonable agreement between the underlying contours of the measured Q_{ext} and the CSW
513 simulations, implying that the fitted n_{532} is good. There is no noticeable hysteresis in the measured
514 Q_{ext} , so there is no effect of inhibition of water transport between the droplet and the gas phase because
515 of increases in viscosity on the timescales of RH variation performed here. The droplet finally fell
516 from the trap at $\sim 3\%$ RH upon the second RH reduction phase. This particle loss could be attributed
517 to efflorescence, but could equally be due to the particle randomly exiting the trap through instability.

518

519 **V. Measurement of Q_{ext} for Accumulation Mode Aerosol**

520 Up until this point we have only presented results for droplets which were larger than ~ 800 nm in
521 radius. As was discussed in the introduction, the most important aerosol particle size regime in terms
522 of atmospheric optics is that for particles with radii >200 nm but <1000 nm. In this section, we report
523 the first single particle Q_{ext} measurements, and companion CSW Mie theory simulations, for particles
524 with radii ranging from 650 nm to as small as ~ 250 nm. For these measurements, aerosol particles

525 were optically trapped in a BB with a core diameter of $\sim 3 \mu\text{m}$ and positioned in the centre of a $\lambda = 532$
526 nm CRD beam for the measurement of Q_{ext} .

527

528 Figure 8(a) shows the time-dependence of the measured radius (black data points) for a hexanetriol
529 droplet evaporating from a radius of 1040 nm to ≤ 300 nm. As the radius of the droplet approaches the
530 wavelength of the illuminating beam (532 nm), size determination of the droplet is unreliable as the
531 PFs become featureless, giving 50 – 100 nm jumps in the fitted radius. Because the evaporation of
532 hexanetriol is well described by the Maxwell mass-flux equation,^{10,19} we fit a third order polynomial
533 through the portion of the data which has been sized well using Mie theory (i.e., for droplet radii > 400
534 nm) and project the radius forwards in time, as shown by the solid red line in Figure 8(a). The
535 measured Q_{ext} data for this droplet, along with CSW Mie theory simulations, are shown in Figure 8(b).
536 The agreement between the CSW Mie theory simulations and the measured Q_{ext} data is excellent, with
537 near-perfect agreement in the positions of resonance peaks even at droplet radii < 400 nm. This good
538 agreement at small particle sizes is emphasised in the inset, which shows an expanded portion of the
539 data in the range 450 – 600 nm, and indicates that the use of a polynomial fit to predict the radius for
540 small sizes was adequate in describing the size of the particle.

541

542 These results represent the first published single particle measurements of Q_{ext} for accumulation mode
543 aerosol. The fitted n_{532} (which takes a constant value for this single-component system) is $1.4823 \pm$
544 0.0002 , which is in reasonable agreement with previous single particle CRDS measurements for
545 hexanetriol at $\lambda = 532$ nm of 1.4782 ± 0.0007 .²⁵ The value measured here agrees particularly well with
546 the determined n_{532} from previously published radiation pressure measurements, which found n_{532} to
547 be 1.482 ± 0.001 .¹⁹ Reasons for the difference in these values might be variations in the RH at which
548 the measurements were performed; however the exact RH probe measurements were not reported in
549 these previous publications.

550

551 The same experimental set-up was used to examine the hygroscopicity of a sub-650 nm aqueous
552 NaNO_3 droplet at ~ 68 % RH which evaporated to a radius < 500 nm at low (~ 2 %) RH, as shown in

553 Figure 9(a). Because the droplet is so small, angular light scattering becomes featureless and sizing
554 accuracy becomes poor. There is a ~ 50 nm jump in the determined radius, as well as unphysical
555 undulations, despite smooth RH variation. Simply, the variation in scattering intensity with angle as
556 recorded in the PF becomes increasingly featureless as the size diminishes, providing little constraint
557 in the fitting of radius and RI. To describe the time variation in the droplet radius in a way which is
558 more representative of the true radius evolution, a Kappa-Köhler dependence of the form:

$$a = a_0 \left(1 + \kappa \frac{a_w}{1 - a_w} \right)^{1/3} \quad \text{Equation 10}$$

559 is fitted to the RH dependence of the size, where a_0 is the radius of the particle at 0 % RH, a_w is the
560 activity of water (which is equal to the RH if the droplet is at equilibrium), and κ is a hygroscopicity
561 parameter. Both κ and a_0 were varied in a least squares fit of Equation 10 to the measured radius and
562 this curve is shown as the black solid line in Figure 9(a). Using this description of radius as a function
563 of RH and thus time, the measured Q_{ext} were calculated for a given w , and fitted to CSW Mie
564 simulations by varying w , $n_{1,532}$ and $n_{2,532}$. The best-fit measured Q_{ext} variation with size and
565 corresponding CSW Mie simulations are plotted in Figure 9(b). The CSW Mie simulations give a
566 reasonable description of the Q_{ext} variation, with the positions of resonance peaks and troughs in Q_{ext}
567 well located. The underlying contour is well described at large particle sizes, but the description
568 becomes poorer at small sizes, indicating that the RI or radius determination is not as well
569 characterised as in previous hygroscopic growth measurements. This trend is expected at small particle
570 sizes as we approach the experimental limits of the measurement where accurate determinations of RI
571 and radius are not possible because the droplet radius is smaller than the illuminating wavelength used
572 for PF acquisition. The accuracy of RI and radius determinations from PFs can be improved for sub-
573 500 nm radius droplets by using a ~ 400 nm illuminating wavelength, as demonstrated in our previous
574 publication.¹⁹

575

576 VI. Conclusions

577 A new experimental approach has been presented for the measurement of single aerosol particle Q_{ext} at
578 a wavelength of 405 nm, combining CRDS ($\lambda = 405$ nm) with BB optical confinement ($\lambda = 532$ nm) in

579 tandem with PF measurements. This technique has been benchmarked using semi-volatile droplets of
580 1,2,6-hexanetriol, allowing Q_{ext} to be measured over a continuous radius range. The measured
581 distribution of Q_{ext} derives from the particle moving within the BB trap over a few microns, traversing
582 several nodes and anti-nodes of the cavity standing wave, with the limits in Q_{ext} accounted for using
583 CSW Mie theory. A residual is defined as the percentage of data points that fall outside the CSW Mie-
584 theory simulation envelope and is minimized to obtain n_{405} . Repeat measurements for 10 evaporating
585 hexanetriol droplets give a mean value for n_{405} of 1.4906 ± 0.0012 , in good agreement with previous
586 determinations from radiation pressure measurements (1.485 ± 0.006).¹⁹

587

588 For hygroscopic inorganic aerosol particles exposed to a decreasing RH, both particle radius and RI
589 change as water partitions from the aerosol particle into the gas phase. A parameterisation of n_{λ} in
590 terms of the particle radius is presented, consisting of 2 or 3 fit parameters (depending on the inorganic
591 species) which are optimised to maximise the mean correlation between the measured PFs and Mie
592 theory simulations. Radius and RI determinations from PFs ($\lambda = 532$ nm) for both an aqueous
593 $(\text{NH}_4)_2\text{SO}_4$ and a NaNO_3 droplet are presented. For both these systems, the determined n_{532} variation
594 with RH agrees well with previous parameterisations by Tang *et al.*, indicating correct n_{532}
595 determination.^{27,34} Best-fit Q_{ext} variation to CSW Mie simulations allows n_{405} to be evaluated. For these
596 simulations, n_{405} was fitted using a parameterisation relating n_{405} to the droplet radius in the same way
597 as performed in the PF fitting procedure. The results show excellent agreement between the resonance
598 peak positions of the measured Q_{ext} and CSW Mie simulations and a good description of the
599 underlying contour of the data. This indicates accurate size determination from fitting the PFs and
600 good n_{405} determination by CRDS. There are no literature parameterisations for the variation in n_{405}
601 with RH for either $(\text{NH}_4)_2\text{SO}_4$ or NaNO_3 with which to compare our results. However, n_{405} is shifted to
602 higher values of RI compared to n_{532} , as expected given typical dispersion behaviour for most
603 materials. Polynomials of the form of Equation 5 were fitted to the measured n_{405} and n_{532} variation
604 with water activity, a_w , for both $(\text{NH}_4)_2\text{SO}_4$ and NaNO_3 . Table 1 summarises the coefficients obtained
605 in these fits. The measured n_{405} variations for both a $(\text{NH}_4)_2\text{SO}_4$ droplet and a NaNO_3 droplet were
606 compared with those predicted using two commonly encountered mixing rules. The volume fraction

607 mixing rule gives poor agreement with the measured n_{405} data, even though extrapolated solute melt
608 densities are used. However, the molar refraction mixing rule gives good agreement with the measured
609 n_{405} data.

610

611 Although the first NaNO_3 droplet reported here was observed to fall out of the BB trap at $\sim 12\%$ RH,
612 many subsequent droplets remained trapped to as low as $\sim 2\%$ RH without undergoing crystallisation.
613 When the RH was kept at $\sim 2\%$ for ~ 40 minutes, and subsequently increased to high RH and to low
614 RH once more, no hysteresis was observed in the measured Q_{ext} , indicating that there is no inhibition
615 of water transport from the aerosol particle to the gas phase on the timescales of the RH variation.

616

617 We present the first single particle measurements of Q_{ext} for accumulation mode aerosol. The measured
618 Q_{ext} variation is shown for a sub-micron hexanetriol droplet evaporating from an initial radius of 1040
619 nm to ≤ 300 nm, which is well within the accumulation mode regime. The radius below ~ 400 nm is
620 poorly determined because the droplet radius is less than the wavelength of light. The evaporation of
621 hexanetriol is described by the Maxwell mass flux equation, allowing extrapolation of a third order
622 polynomial fitted to the >400 nm radius data. The agreement between the measured Q_{ext} and the fitted
623 CSW Mie simulations is good, even at small radii where the droplet radius has been predicted using
624 the polynomial extrapolation. Finally, the hygroscopicity of a sub- 650 nm NaNO_3 droplet is studied as
625 it evaporates and shrinks to a radius < 500 nm at low ($\sim 2\%$) RH. The radius determination by PF
626 analysis is poor in this size regime. Using the measured RH variation, a Kappa Köhler curve is fitted
627 to the radius data to describe the radius evolution. Using this description for radius, the Q_{ext} variation
628 with size is presented along with best fit CSW Mie simulations. These simulations give a reasonable
629 description of the measured Q_{ext} variation. The limitations in the radius determination by PF analysis
630 might be improved by using a shorter wavelength laser source to illuminate the droplet.

631

632 **Acknowledgements**

633 JPR acknowledges financial support from the EPSRC through a Leadership Fellowship
634 (EP/G007713/1). MIC acknowledges funding from NERC and the RSC through an Analytical Trust

635 Fund studentship and support from the Aerosol Society in the form of a CN Davies award. BJM
636 acknowledges the EPSRC for funding. We thank NERC for financial support for instrument
637 development via grant NE/H001972/1.

638

639 **References**

- 640 1. J. Julin, M. Shiraiwa, R. E. H. Miles, J. P. Reid, U. Pöschl, and I. Riipinen, *The Journal of*
641 *Physical Chemistry A*, 2013, **117**, 410–20.
- 642 2. R. E. H. Miles, A. E. Carruthers, and J. P. Reid, *Laser & Photonics Reviews*, 2011, **5**, 534–552.
- 643 3. B. J. Mason, S.-J. King, R. E. H. Miles, K. M. Manfred, A. M. J. Rickards, J. Kim, J. P. Reid,
644 and A. J. Orr-Ewing, *The Journal of Physical Chemistry. A*, 2012, **116**, 8547–8556.
- 645 4. J. Michel Flores, R. Z. Bar-Or, N. Bluvshstein, A. Abo-Riziq, A. Kostinski, S. Borrmann, I.
646 Koren, and Y. Rudich, *Atmospheric Chemistry and Physics*, 2012, **12**, 5511–5521.
- 647 5. A. R. Attwood and M. E. Greenslade, *The Journal of Physical Chemistry A*, 2012, **116**, 4518–
648 4527.
- 649 6. E. Dinar, A. Abo Riziq, C. Spindler, C. Erlick, G. Kiss, and Y. Rudich, *Faraday Discussions*,
650 2008, **137**, 279–295.
- 651 7. N. Lang-Yona, Y. Rudich, E. Segre, E. Dinar, and A. Abo-Riziq, *Analytical Chemistry*, 2009,
652 **81**, 1762–9.
- 653 8. D. Mellon, S. J. King, J. Kim, J. P. Reid, and A. J. Orr-Ewing, *The Journal of Physical*
654 *Chemistry A*, 2011, **115**, 774–83.
- 655 9. L. Alexander, S. Allen, N. Bindoff, F.-M. Breon, J. Church, U. Cubasch, S. Emori, P. Forster,
656 P. Friedlingstein, N. Gillett, Jonathan Gregory, D. Hartmann, E. Jansen, B. Kirtman, R. Knutti,
657 K. K. Kanikicharla, P. Lemke, Jochem Marotzke, V. Masson-Delmotte, G. Meehl, I. Mokhov,
658 S. Piao, V. Ramaswamy, D. Randall, M. Rhein, M. Rojas, C. Sabine, D. Shindell, L. Talley, D.
659 Vaughan, and S.-P. Xie, *Climate Change 2013 : The Physical Science Basis - Working Group I*
660 *Contribution to the IPCC Fifth Assessment*, .
- 661 10. U. K. Krieger, C. Marcolli, and J. P. Reid, *Chemical Society Reviews*, 2012, **41**, 6631–62.

- 662 11. J. F. Davies, A. E. Haddrell, and J. P. Reid, *Aerosol Science and Technology*, 2012, **46**, 666–
663 677.
- 664 12. J. F. Davies, A. E. Haddrell, A. M. J. Rickards, and J. P. Reid, *Analytical Chemistry*, 2013, **85**,
665 5819–5826.
- 666 13. R. E. H. Miles, J. S. Walker, D. R. Burnham, and J. P. Reid, *Physical Chemistry Chemical*
667 *Physics*, 2012, **14**, 3037–47.
- 668 14. R. M. Power, S. H. Simpson, J. P. Reid, and A. J. Hudson, *Chemical Science*, 2013, **4**, 2597–
669 2604.
- 670 15. J. Durnin and J. J. Miceli, *Physical Review Letters*, 1987, **58**, 1499–1501.
- 671 16. J. Durnin, *Journal of the Optical Society of America A*, 1987, **4**, 651–654.
- 672 17. J. Durnin, J. J. Miceli, and J. H. Eberly, *Optics letters*, 1988, **13**, 79.
- 673 18. A. E. Carruthers, J. S. Walker, A. Casey, A. J. Orr-Ewing, and J. P. Reid, *Physical Chemistry*
674 *Chemical Physics*, 2012, **14**, 6741–6748.
- 675 19. M. I. Cotterell, B. J. Mason, A. E. Carruthers, J. S. Walker, A. J. Orr-Ewing, and J. P. Reid,
676 *Physical Chemistry Chemical Physics*, 2014, **16**, 2118–28.
- 677 20. J. S. Walker, A. E. Carruthers, A. J. Orr-Ewing, and J. P. Reid, *The Journal of Physical*
678 *Chemistry Letters*, 2013, **4**, 1748–1752.
- 679 21. D. McGloin and K. Dholakia, *Contemporary Physics*, 2005, **46**, 15–28.
- 680 22. A. E. Carruthers, J. P. Reid, and A. J. Orr-Ewing, *Optics Express*, 2010, **18**, 14238–44.
- 681 23. J. W. Lu, M. Isenor, E. Chasovskikh, D. Stapfer, and R. Signorell, *The Review of Scientific*
682 *Instruments*, 2014, **85**, 095107.
- 683 24. I. Thanopoulos, D. Luckhaus, T. C. Preston, and R. Signorell, *Journal of Applied Physics*, 2014,
684 **115**, 154304.
- 685 25. B. J. Mason, J. S. Walker, J. P. Reid, and A. J. Orr-Ewing, *The Journal of Physical Chemistry*
686 *A*, 2014.
- 687 26. J. P. Reid, B. J. Mason, M. I. Cotterell, T. C. Preston, and A. J. Orr-Ewing, *SPIE Proceedings*,
688 2014, **9164**.
- 689 27. I. N. Tang and H. R. Munkelwitz, *Journal of Geophysical Research*, 1994, 18801–18808.

- 690 28. T. J. A. Butler, J. L. Miller, and A. J. Orr-Ewing, *The Journal of Chemical Physics*, 2007, **126**,
691 174302.
- 692 29. H. Kogelnik and T. Li, *Proceedings of the IEEE*, 1966, **54**, 1312–1329.
- 693 30. J. L. Miller and A. J. Orr-Ewing, *The Journal of Chemical Physics*, 2007, **126**, 174303.
- 694 31. J. P. Reid and L. Mitchem, *Annual Review of Physical Chemistry*, 2006, **57**, 245–71.
- 695 32. T. C. Preston and J. P. Reid, *Optics Express*, 2015, submitted.
- 696 33. P. R. Bevington and D. K. Robinson, *Data Reduction and Error Analysis for the Physical*
697 *Sciences*, McGraw-Hill, 3rd edn., 2003.
- 698 34. I. N. Tang, A. C. Tridico, and K. H. Fung, *Journal of Geophysical Research*, 1997, **102**,
699 23269–23275.
- 700 35. J. W. Lu, A. M. J. Rickards, J. S. Walker, K. J. Knox, R. E. H. Miles, J. P. Reid, and R.
701 Signorell, *Physical Chemistry Chemical Physics*, 2014, **16**, 9819–9830.
- 702 36. M. Daimon and A. Masumura, *Applied Optics*, 2007, **46**, 3811–3820.
- 703 37. Q.-N. Zhang, Y. Zhang, C. Cai, Y.-C. Guo, J. P. Reid, and Y.-H. Zhang, *The Journal of*
704 *Physical Chemistry A*, 2014, **118**, 2728–2737.
- 705 38. M. Gysel, E. Weingartner, and U. Baltensperger, *Environmental Science Technology*, 2002,
706 63–68.
- 707 39. Y. Liu and P. H. Daum, *Journal of Aerosol Science*, 2008, **39**, 974–986.
- 708 40. J. L. Hand and S. M. Kreidenweis, *Aerosol Science and Technology*, 2002, **36**, 1012–1026.
- 709 41. S. L. Clegg and A. S. Wexler, *The Journal of Physical Chemistry A*, 2011, 3393–3460.
- 710 42. S. L. Clegg, P. Brimblecombe, and A. S. Wexler, *The Journal of Physical Chemistry A*, 1998,
711 **102**, 2155–2171.
- 712 43. *ADIENT database*: <http://www.met.rdg.ac.uk/adient/refractiveindices.html>.
- 713

714

TABLES

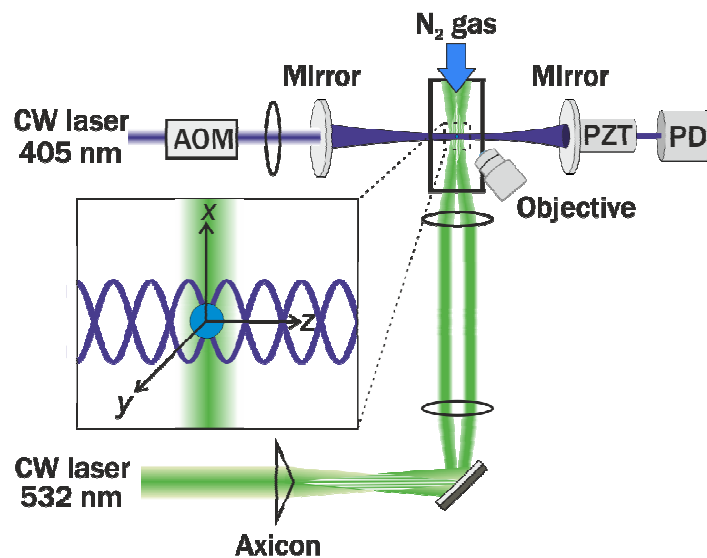
	$(\text{NH}_4)_2\text{SO}_4$		NaNO_3	
	$\lambda = 532 \text{ nm}$	$\lambda = 405 \text{ nm}$	$\lambda = 532 \text{ nm}$	$\lambda = 405 \text{ nm}$
C_0	1.476	1.526	1.481	1.504
C_1	-9.748×10^{-2}	-1.547×10^{-1}	-1.166×10^{-1}	-9.947×10^{-2}
C_2	1.501×10^{-1}	2.032×10^{-1}	-1.233×10^{-1}	-2.184×10^{-1}
C_3	-1.621×10^{-1}	-1.973×10^{-1}	3.490×10^{-1}	4.973×10^{-1}
C_4	-	-	-2.613×10^{-1}	-3.482×10^{-1}

715

716 **Table 1:** Summary of the determined coefficients for calculating the RI from water activity, a_w , using Equation 5717 for the inorganic species $(\text{NH}_4)_2\text{SO}_4$ and NaNO_3 , at illuminating wavelengths of 405 and 532 nm.

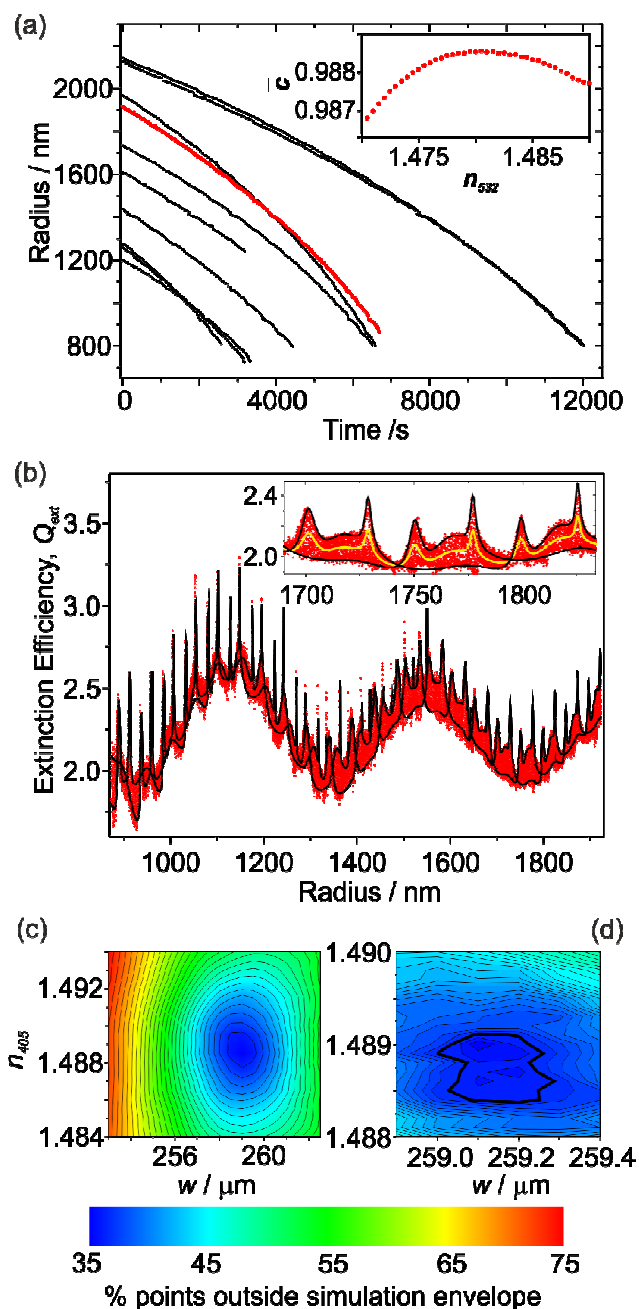
718 FIGURES

719



720

721 **Figure 1.** Schematic diagram of the apparatus used to perform CRDS on single aerosol particles optically
722 trapped in a BB. AOM is an acousto-optic modulator, PZT is a piezoelectric transducer, PD is a photodiode. The
723 inset defines the coordinate system used in CSW Mie theory calculations and shows a particle confined in a BB
724 core intersected with the intra-cavity standing wave.



725

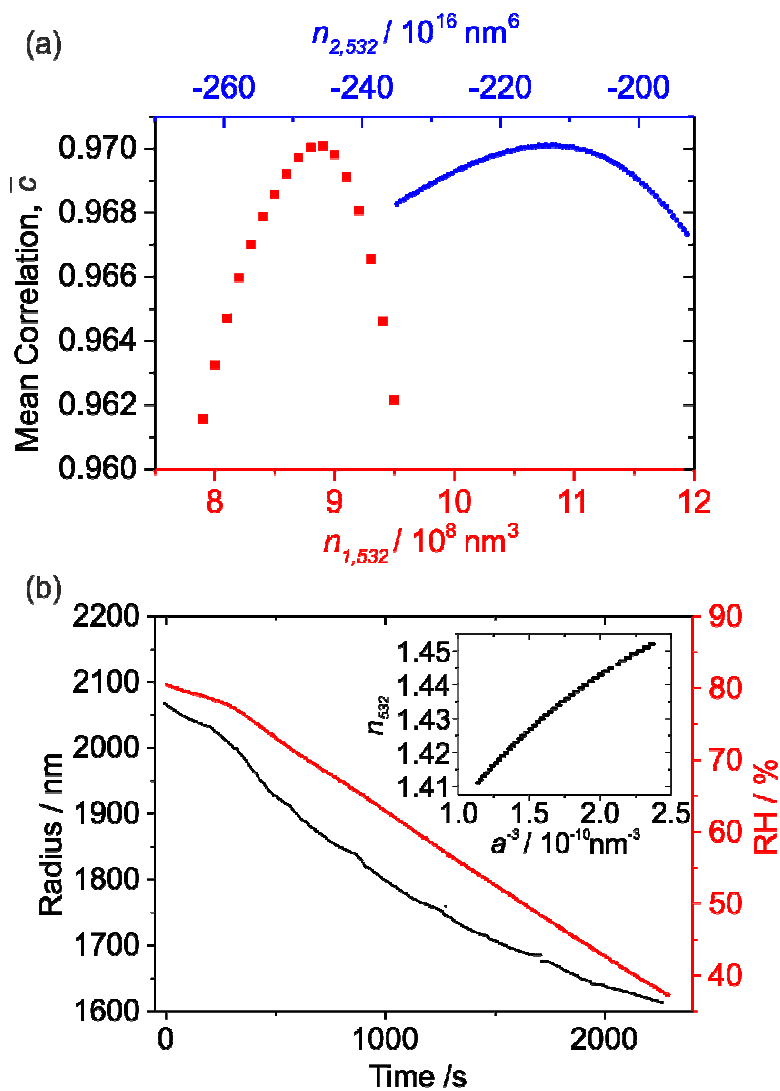
726 **Figure 2:** (a) The measured radius vs time for ten 1,2,6-hexanetriol droplets. The inset shows the mean727 correlation coefficient, \overline{C} , between the measured and simulated PFs as a function of n_{532} for the radius data728 plotted with red data points. (b) The measured Q_{ext} for the radius data plotted in red in (a), along with the best fit

729 CSW Mie simulation. The inset shows an expanded portion, highlighting the good agreement between the

730 boundaries in the measured Q_{ext} and the CSW Mie simulations, along with a conventional Mie simulation (solid

731 yellow line). (c) A contour plot of the percentage of points outside the CSW Mie simulation envelope as a

732 function of the two fitting parameters, n_{405} and w . (d) An expanded portion of the contour plot in (c).



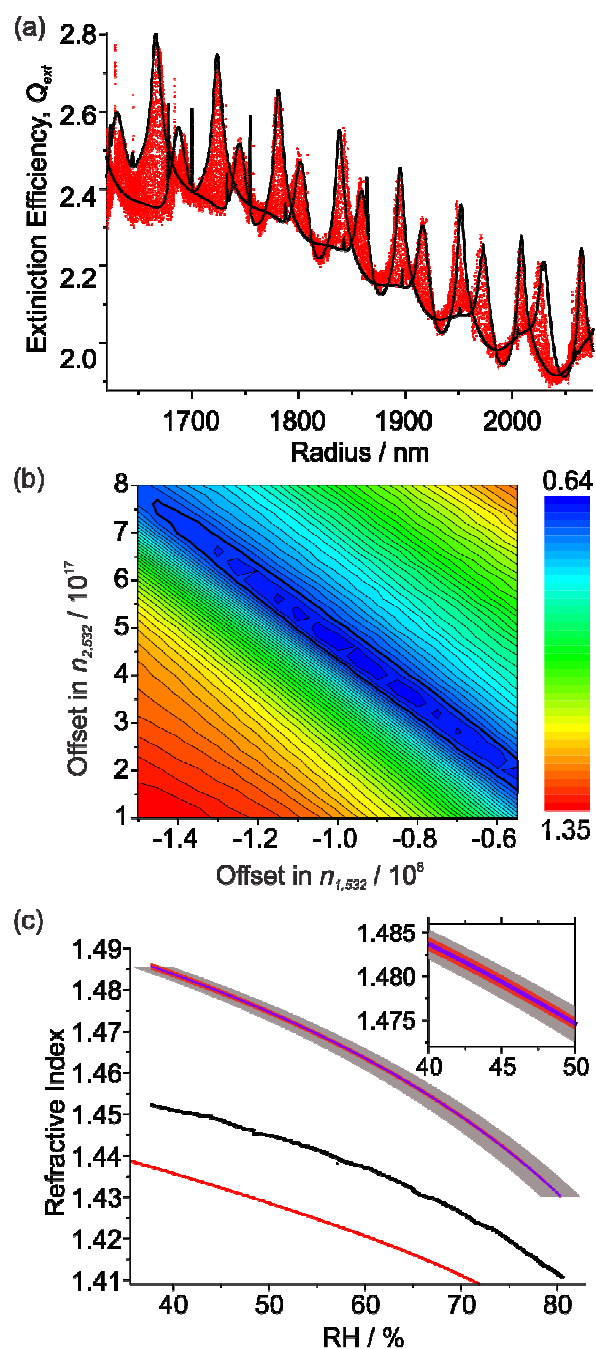
733

734 **Figure 3:** (a) The mean correlation, \bar{C} , as a function of $n_{1,532}$ (red squares) and $n_{2,532}$ (blue circles) during the

735 initial stages of their optimisation through PF fitting for a hygroscopic growth measurement of ammonium

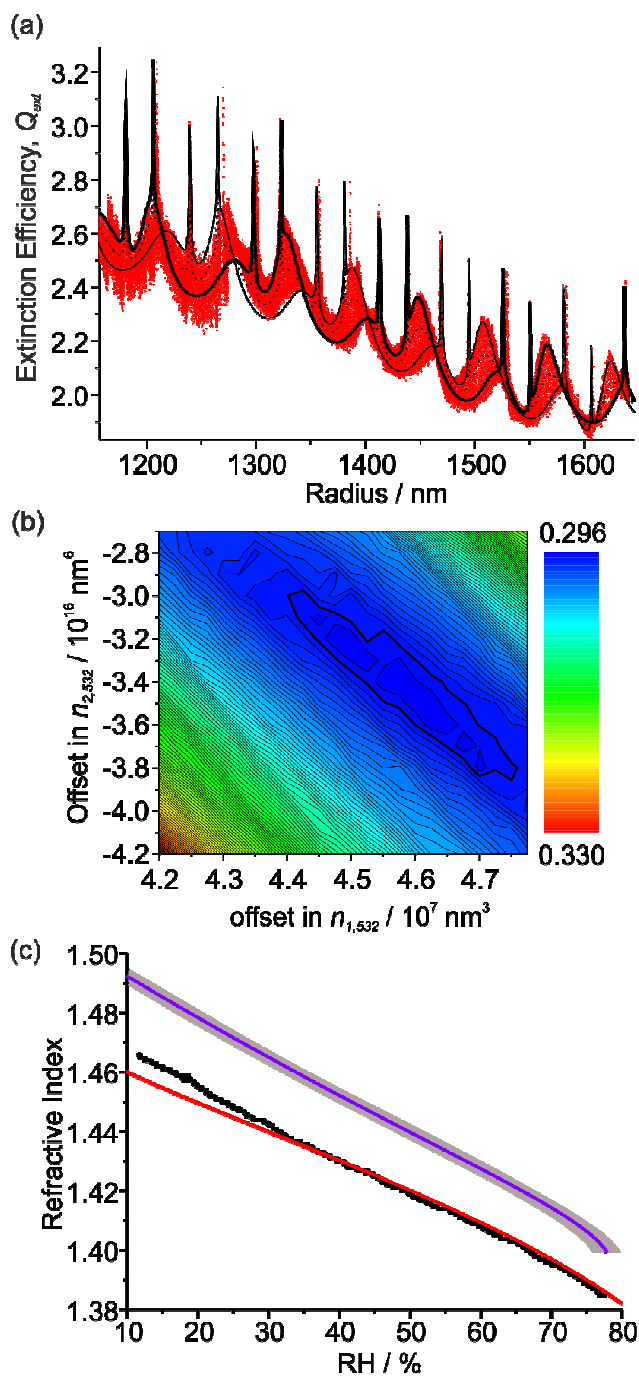
736 sulfate. (b) The measured RH vs time and determined radius vs time for the ammonium sulfate droplet in (a).

737 The inset shows how the determined RI at 532 nm varies with a^{-3} .



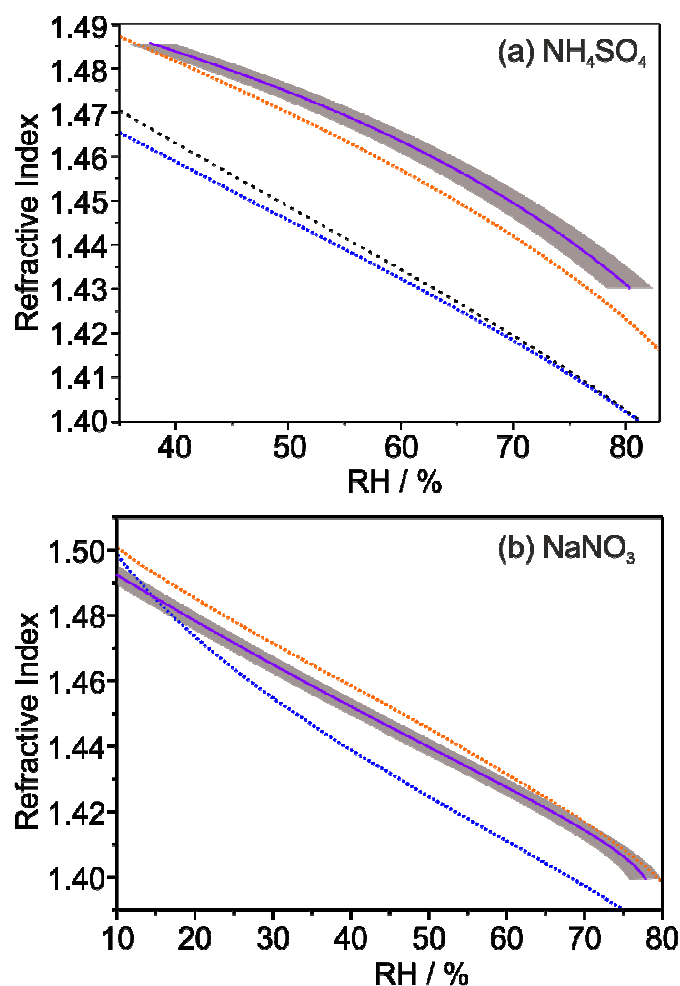
738

739 **Figure 4:** – (a) The measured Q_{ext} variation with particle radius for the hygroscopic growth of the $(\text{NH}_4)_2\text{SO}_4$
 740 droplet in Figure 3 (red data points) and best-fit CSW Mie simulations (black lines). (b) Contour plot of the
 741 dependence of the residual on Δn_1 and Δn_2 . (c) RH dependence of n_{532} (black data points) and n_{405} (purple
 742 line), with a comparison to the parameterisation of Tang *et al.* ($\lambda = 633$ nm, red line).^{27,34} The red envelope
 743 shows the uncertainty in n_{405} resulting from uncertainties in Δn_1 and Δn_2 . The larger grey envelope shows the
 744 uncertainty caused by uncertainty in the RH measurement. The inset shows an expanded portion of these
 745 envelopes.



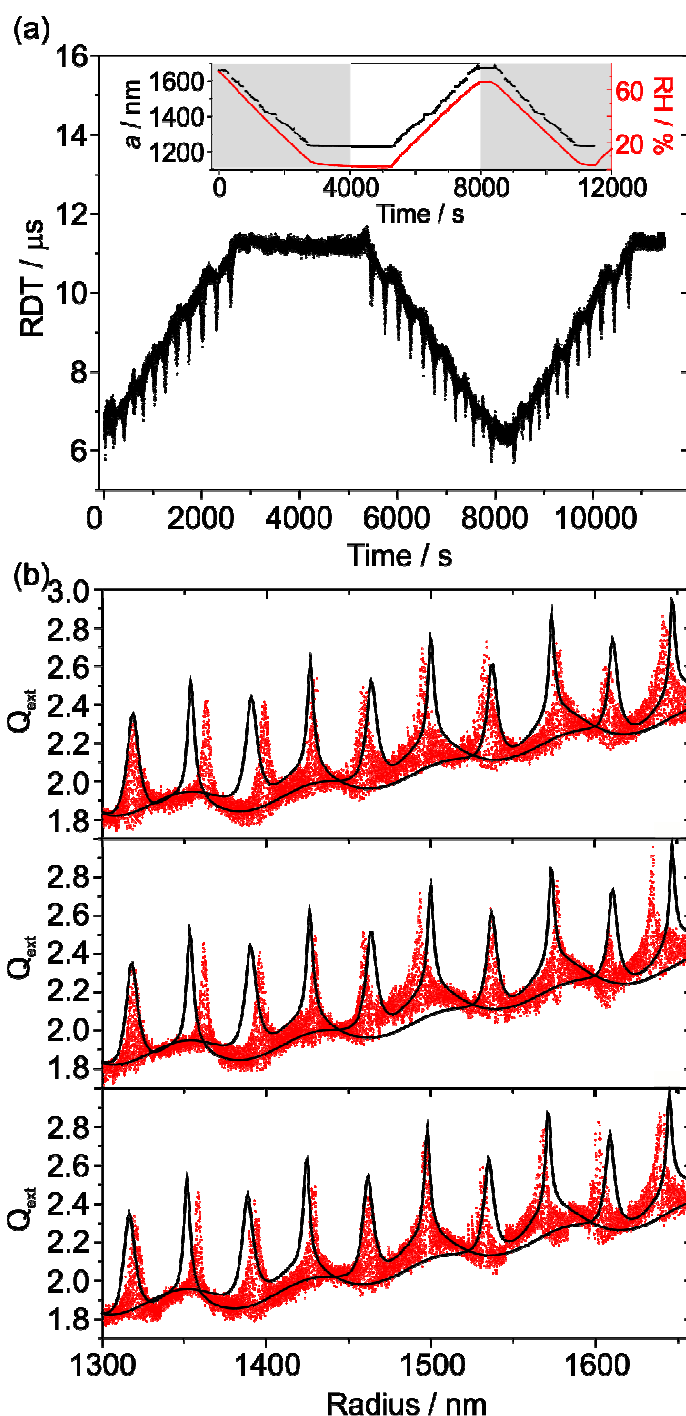
746

747 **Figure 5:** - (a) The measured Q_{ext} variation with particle radius for the hygroscopic growth of a NaNO_3 droplet
 748 (red data points) and best-fit CSW Mie simulations (black lines). (b) Contour plot of the dependency of the
 749 residual on Δn_1 and Δn_2 . (c) The determined RH dependence of n_{532} (black data points) and n_{405} (purple line),
 750 with a comparison to the parameterisation of Tang *et al.* ($\lambda = 633 \text{ nm}$, red line).^{27,34} The large grey envelope
 751 shows the uncertainty caused by uncertainty in the RH measurement.



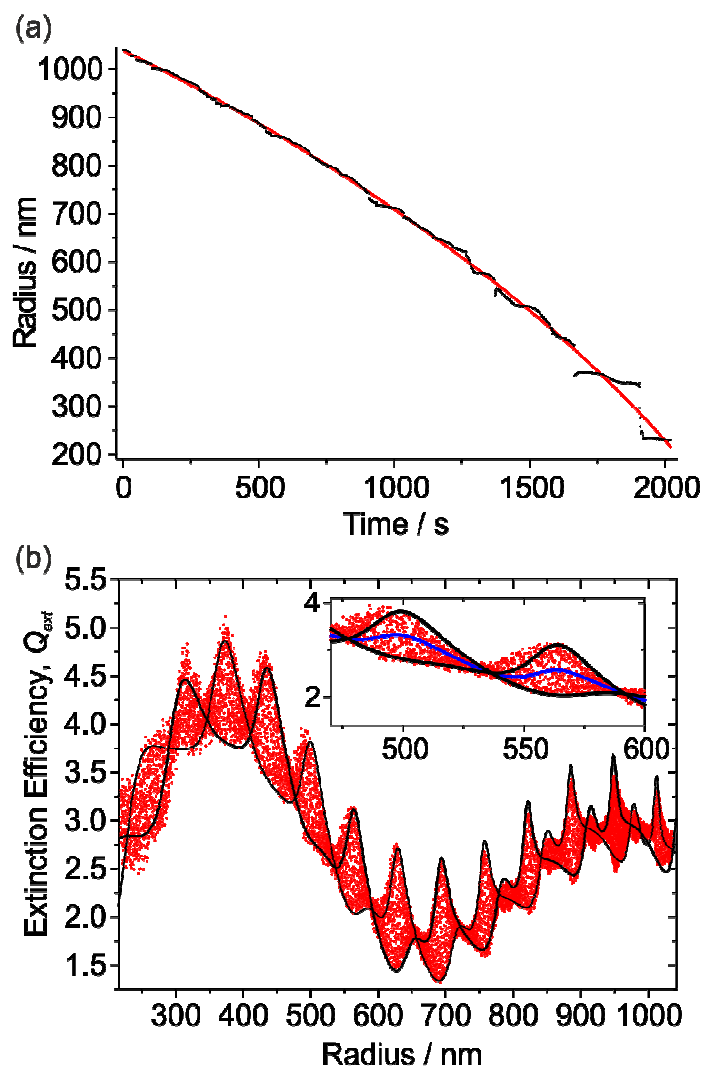
752

753 **Figure 6:** Comparison of predictions from mixing rules with the measured n_{405} variation with RH (solid purple
 754 line) for (a) ammonium sulfate and (b) sodium nitrate. The grey envelopes show a $\pm 2\%$ uncertainty in the RH
 755 probe measurement. The dashed orange lines show the predictions of the molar refraction mixing rule, while the
 756 dashed blue lines show the conventional volume fraction mixing rule predictions, taking n_{405} of water to be 1.343
 757 and n_{405} for the pure, inorganic liquid melt to be equal to the corresponding C_0 value in
 758 Table 1. The densities of the pure, inorganic melt are described using the model of Clegg and Wexler.⁴¹ The
 759 dashed black line in (a) shows the prediction of the volume fraction mixing rule when the crystalline ammonium
 760 sulfate density (1.769 g cm^{-3}) is used with the ADIENT value of n_{405} (1.54) for pure ammonium sulfate.⁴³



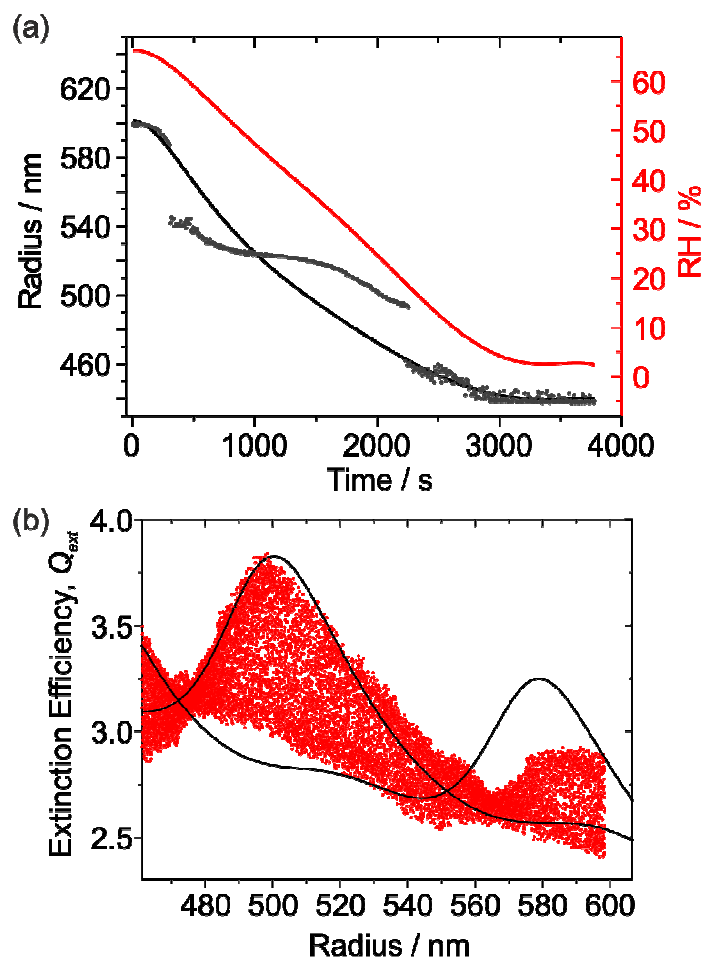
761

762 **Figure 7:** (a) The measured RDTs over time for a NaNO_3 droplet in an experiment in which the RH was cycled
 763 between low and high RH. The inset shows how the RH and droplet radius varied over time, while the shaded
 764 panels demark regions where the Q_{ext} were determined separately. (b) The determined Q_{ext} as a function of radius
 765 for the three regions highlighted in the inset of (a), with accompanying CSW Mie simulations.



766

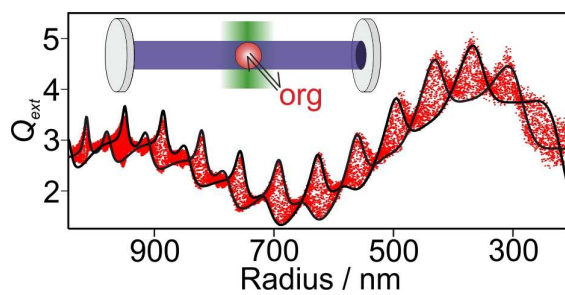
767 **Figure 8:** (a) The determined radius as a function of time for a hexanetriol droplet which evaporates to
768 accumulation mode sizes. A 3rd order polynomial is fitted to data > 400 nm, and extrapolated to smaller radii
769 (longer times). (b) The result of Q_{ext} fitting to CSW Mie simulations, using the radius determination from the
770 third order polynomial fit.



771

772 **Figure 9:** (a) Plot of the measured radius vs time (grey data points) for a hygroscopic growth experiment on a
773 small sodium nitrate droplet, with the RH variation also plotted (red solid line). Also shown is a fit of a Köhler-
774 Köhler curve to the radius data (black solid line). (b) Measured Q_{ext} with accompanying best fit CSW Mie theory
775 simulations.

776

777 **Table of Contents Graphic**

778

779 We report a new single aerosol particle approach using cavity ringdown spectroscopy to accurately

780 determine optical extinction cross-sections at multiple wavelengths.